1

Introduction

1.1 High-power GaAs-based broad-area diode lasers

Since the first demonstrations of lasing in the early 1960s and the subsequent realization of different types of laser devices, the field has evolved into an ever-growing multi-billion-dollar market, with a revenue reaching $17 billion in 2020 and projected to experience 10% annual growth to reach ∼$28 billion by 2025 [1]. This remarkable market growth has been enabled by continuous performance improvements of laser devices as the corresponding technologies matured, leading to their utilization in a wide array of applications. As shown in Fig. 1.1, the largest of these applications is industrial manufacturing and materials processing, representing roughly one-third of total revenue in 2020. The second largest application in terms of revenue is communications, followed by aerospace and defence, having the highest projected annual growth rate, in addition to sensing (e.g. LIDAR), electronics manufacturing (e.g. lithography), and medical applications, among others.

Among the different types of laser devices, semiconductor diode lasers are the most widely used, constituting a 39–40% share of total revenue, as shown in Fig. 1.1. This is attributed to diode lasers having favorable properties in comparison to other device types, one of which is being electrically rather than optically pumped, which enables higher power conversion efficiencies. Modern diode lasers also demonstrate high reliability and long lifetime, enabled by progress in crystal growth, processing technology, facet passivation and chip packaging (see section 2.2). In addition, they are relatively inexpensive, making use of wafer-scale processing for mass production, and tend to have smaller component size, even after packaging [2,3]. Since their first realization in 1962 [4], many variations of diode lasers have been developed and realized, making use of different material systems to extend the range of emission wavelength (λ), as well as different device configurations, e.g. edge-emitting ridge waveguide lasers and vertical-cavity surface-emitting lasers (VCSELs), each offering certain desirable performance characteristics that make them ideal for specific applications. For applications that require high optical power levels, the most widely-used variant is edge-emitting broad-area diode lasers (BALs) based on gallium arsenide (GaAs), which are the subject of this work.

Figure 1.2 shows a schematic diagram of a standard high-power BAL with stripe width W and resonator length L, with the output laser beam emitted from its front facet. The

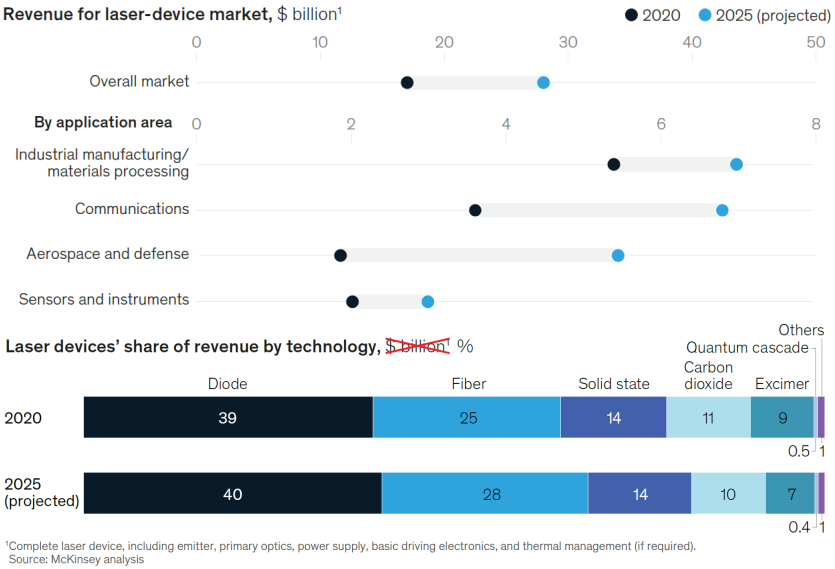

Figure 1.1: Metrics and future trends of the global laser device market (adapted from [1]): total revenues (in $ billion) of the overall market and the four largest application areas in 2020 and their projected growth up to 2025 (top), and relative shares of the total revenue (in %) of the different laser device types in 2020 and the corresponding projected values in 2025 (bottom). (©McKinsey and Company)

steps involved in the fabrication of these devices are presented in section 2.2, with the final configuration providing mechanisms for optical mode guiding and electrical charge carrier confinement in the three directions (vertical, lateral and longitudinal). The vertical layer structure of the diode laser is epitaxially grown on a GaAs substrate, and includes an active zone at the p-n-junction with thickness d_{AZ}, typically containing one or multiple quantum wells (QWs), each with a thickness of few nm. Lasing (light generation) takes place inside these QWs, with λ determined by their material composition, thickness and incorporated strain. The optical guiding of generated light in the vertical direction is enabled by the layers surrounding the active zone on the n- and p-sides, namely waveguide layers (with higher refractive index) surrounded by cladding layers (with lower refractive index). In the lateral direction, W is defined by lateral structuring techniques based on selective ion implantation and/or etching, in some cases involving buried structures via multi-step epitaxial growth (see chapter 3). Finally, in the longitudinal direction, mirror facets are formed by cleaving BALs along crystal planes of the wafer, thus defining a Fabry-Pérot resonator with length L, followed by passivation to improve facet stability and coating to set the reflectivities of the front and rear facets (typically 0.5–5% and 95–98%, respectively) [5–8].

GaAs-based BALs offer the highest optical power (P_{opt}) among diode lasers and the highest power conversion efficiency (η_{E}) among all light sources. η_{E} is defined as the ratio of output

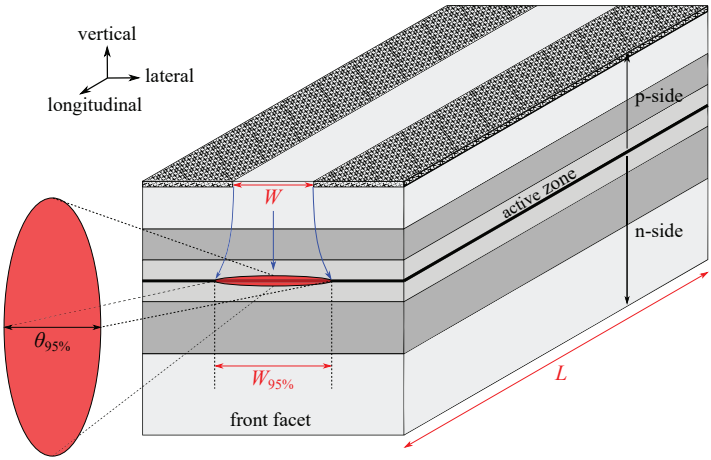

Figure 1.2: Three-dimensional schematic diagram of a standard high-power broad-area diode laser with stripe width W and resonator length L, where lasing (light generation) takes place inside the active zone at the p-n-junction, and the output laser beam is emitted from the front facet. The lateral beam parameters, namely near-field width ($W_{95\%}$) and far-field angle ($\theta_{95\%}$) with 95% power content, as well as the current path inside the device are indicated on the diagram.

(optical) to input (electrical) power, i.e.

$$\eta_{\mathrm{E}} = \frac{P_{\mathrm{opt}}}{I \cdot U} = \frac{P_{\mathrm{opt}}}{I \cdot (U_0 + R_{\mathrm{s}} I)}, \tag{1.1}$$

where I is the operating (bias) current and $U = U_0 + R_{\mathrm{s}} I$ is the operating voltage, with U_0 as the turn-on voltage and R_{s} as the series resistance [2,8]. In these devices, the vertical structure is grown on a GaAs substrate, with all the epitaxial layers made of binary, ternary and quaternary materials from the (AlGaIn)(AsP) III-V compound semiconductor family [6]. This wide variety of available material systems allows the realization of GaAs-based BALs with a very wide range of λ, roughly between 630 and 1200 nm, although peak P_{opt} and η_{E} are significantly lower at the extremes [9]. High peak $\eta_{\mathrm{E}} > 70\%$ has been reported from GaAs-based BALs over the λ range between 790 and 1060 nm, with the highest P_{opt} levels to date achieved in the 9xx nm range [9,10].

As a result, these high-power GaAs-based BALs operating in the 9xx nm range are widely used in material processing applications, such as metal cutting and welding and additive manufacturing, where they are either used to optically pump solid-state and fiber lasers (e.g. Yb-doped fiber laser), or directly utilized in so-called direct diode laser systems [3,9]. In addition to high P_{opt} and η_{E}, these applications also require high brightness, i.e. maintaining high beam quality at high P_{opt}. Beam quality essentially refers to the smallest spot size into which the laser beam can be focused, and can thus significantly affect the coupling efficiency of the generated P_{opt} into a given optical system. For example, for pumping a fiber with a specific core diameter and numerical aperture, low beam quality of the BAL source can limit the amount of useful P_{opt} coupled into the fiber, thus reducing the overall system efficiency [3]. The

beam shape in near- and far-field regions of a high-power BAL is schematically illustrated in Fig. 1.2. The vertical waveguide is typically designed to exclusively guide a single (fundamental) mode, which leads to the output beam having an almost diffraction-limited profile along the vertical (fast) axis, i.e. very high vertical beam quality, despite the strong divergence shown in the diagram. Conversely, the output beam profile along the lateral (slow) axis deviates strongly from the ideal diffraction-limited case, corresponding to limited lateral beam quality, due to the broad stripe allowing the guiding of a large number of modes. Lateral beam quality is typically quantified in terms of the lateral beam parameter product (BPP_{lat}), which is defined as

$$BPP_{\mathrm{lat}} = 0.25 \times W_{95\%} \times \theta_{95\%}, \tag{1.2}$$

where $W_{95\%}$ is the lateral near-field width (beam waist) and $\theta_{95\%}$ is the lateral far-field angle (divergence angle), both including 95% of the optical power content (see Fig. 1.2). For improving lateral beam quality, $W_{95\%}$ and $\theta_{95\%}$ should be minimized, corresponding to lower BPP_{lat}. P_{opt} and BPP_{lat} can be combined into one key BAL performance metric, namely lateral brightness (B_{lat}), which is defined as

$$B_{\mathrm{lat}} = \frac{P_{\mathrm{opt}}}{BPP_{\mathrm{lat}}}. \tag{1.3}$$

The demand for 9xx nm BALs with ever-higher power, efficiency and brightness remains high, with the aim of realizing material processing systems with enhanced capabilities and reduced operation costs, in addition to enabling new applications. Ongoing efforts to develop novel BAL designs with enhanced performance in terms of P_{opt}, η_{E} and B_{lat} are therefore highly beneficial and commercially valuable.

The peak performance achievable by a single BAL emitter (as shown in Fig. 1.2) is strongly dependent on its dimensions and vertical structure, as well as the operating conditions. BALs with W in the 90–120 µm range are typical, as they tend to exhibit the best overall performance. However, broader stripes with W as high as 1200 µm have been used to achieve higher P_{opt} while maintaining high η_{E}, but this comes at the expense of increased BPP_{lat} and thus lower peak B_{lat}. Conversely, narrower stripes with W as low as 20 µm can be used to maximize B_{lat} at the expense of P_{opt} and η_{E} [9]. Typical values of L are in the 1–6 mm range, with reported values up to 10 mm. Increasing L in BALs reduces thermal resistance (R_{th}), corresponding to enhanced heat extraction (see section 2.3), which enables higher B_{lat}. However, this comes at the expense of higher threshold current (I_{th}) and lower peak η_{E} [9,11]. Up to a certain L (around 4 mm), the reduced R_{th} also enables higher peak P_{opt}, but with further increase of L, this benefit is limited by the increasing asymmetry of the longitudinal optical profile (longitudinal spatial hole burning; see subsection 3.2.2), which contributes to power saturation and can thus have the opposite effect of reducing peak P_{opt} [12,13]. Similar trade-offs are also involved in the vertical structure design of high-power BALs. For example, it is mentioned above that high vertical beam quality is typically achieved by designing the vertical waveguide for single mode operation. It is usually desirable for this fundamental mode to have a limited overlap with the active zone, i.e. a high d_{AZ}/Γ ratio, where Γ is the optical confinement factor with a value typically lower than 1.5% [3,14]. This is necessary in modern high-power BALs with large L in order to reduce internal optical losses (α_{i}), with the aim of maintaining high η_{E}

and reducing the risk of catastrophic optical mirror damage (COMD), thus improving reliability and enabling higher P_{opt} levels. However, reducing Γ corresponds to lower modal gain, therefore having the disadvantage of increasing I_{th}. In the presence of many such trade-offs, an optimized vertical structure is thus crucial for enhancing the peak performance of high-power BALs. State-of-the-art BALs with typical dimensions of $W = 100\,\mu\mathrm{m}$ and $L = 3$–$5\,\mathrm{mm}$ have exhibited peak P_{opt} levels around 25 W under continuous-wave (CW) operation. However, operating under pulsed conditions enables much higher P_{opt} from the same devices, with short pulses reaching up to 145 W [9,13–15]. In addition, peak performance is strongly affected by the used mounting configuration and cooling technique, as well as the operating heat-sink temperature (T_{HS}) [12,16–18].

For many material processing applications, the power and brightness requirements are far beyond the capabilities of a single BAL emitter, which are limited by the degradation of η_{E} and BPP_{lat} at higher P_{opt} and heat levels. This necessitates the use of beam combining techniques, which enable P_{opt} scaling by combining the output beams of multiple BALs, ideally with no beam quality penalty and thus proportional scaling of brightness. Depending on application requirements, different beam combining techniques can be used, often with a trade-off between simplicity and the properties of the output (combined) beam, which can enable P_{opt} scaling up to the kW range. These techniques include spatial beam combining using bar or stack configurations, spectral beam combining of multiple laser beams (from individual BALs) with slightly varying λ, and coherent beam combining based on controlling the relative phases of multiple laser beams with identical λ to obtain constructive interference, which is the most challenging to implement but offers the highest beam quality [19–22]. A further widely-used technique is polarization beam combining (PBC); a relatively simple technique which enables (up to) two-fold P_{opt} scaling with no beam quality penalty. In PBC, two linearly-polarized beams with mutually perpendicular polarization states, i.e. tranverse electric (TE) and transverse magnetic (TM) polarization, are combined using a polarizing beam splitter [20–23]. One of the key factors that determine the polarization state of a BAL output beam is the aforementioned strain incorporated into QWs during their growth, which splits valence band degeneracy by separating the heavy-hole and light-hole subbands, thus favoring light emission with a specific polarization. For example, GaAs-based 9xx nm BALs are realized using $\mathrm{In}_x\mathrm{Ga}_{1-x}\mathrm{As}$ QWs, which are compressively strained due to having a larger lattice constant than GaAs. This results in heavy-hole transitions having the lowest energy, which corresponds to TE polarization being favored, i.e. with the electric field oscillating in the QW plane [2,23]. To apply PBC on two beams with identical polarization (e.g. output beams of two 9xx nm BAL emitters), a half-wave plate can be used to rotate the orientation of one of them by 90°, thereby changing its polarization state. To minimize combining losses and achieve high PBC efficiency, the beams must have high polarization purity, typically quantified in terms of the degree of polarization (DoP). For BALs with predominantly TE-polarized output beams, DoP is commonly defined as [22–25]

$$DoP = \frac{P_{\mathrm{opt,TE}}}{P_{\mathrm{opt,TE}} + P_{\mathrm{opt,TM}}}, \tag{1.4}$$

where $P_{\mathrm{opt,TE}}$ and $P_{\mathrm{opt,TM}}$ are the TE- and TM-polarized optical powers, respectively. It is sometimes alternatively defined as [26]

$$DoP^{*} = \frac{P_{\mathrm{opt,TE}} - P_{\mathrm{opt,TM}}}{P_{\mathrm{opt,TE}} + P_{\mathrm{opt,TM}}}, \tag{1.5}$$

but unless stated otherwise, the former definition (Eq. 1.4) is used by default in this work. Along with maximizing P_{opt}, η_{E} and B_{lat}, efforts to maintain high DoP and avoid its degradation in novel BAL realizations are also highly important, especially due to the wide use of PBC in industrial systems.

1.2 Scope and structure of this work

As discussed earlier, the development of novel concepts for improved designs of 9xx nm BALs remains highly beneficial and commercially valuable, with the aim of enabling enhanced BAL performance in terms of P_{opt}, η_{E}, and BPP_{lat} (and thus B_{lat}), while maintaining high DoP. This is the motivation and objective of this work, carried out at the Ferdinand-Braun-Institut gGmbH, Leibniz-Institut für Höchstfrequenztechnik (FBH), with specific focus on novel design approaches based on lateral structuring. In the following, the content and structure of the work are described.

Chapter 2 provides an overview of the methods and techniques used to study, realize, and evaluate BALs in this work. It starts by introducing the device modeling and simulation software used for design optimization and performance estimation. It then reviews the fabrication technology used to realize BALs, starting with epitaxial wafer growth, followed by wafer processing, facet passivation and coating, and device mounting and packaging. Finally, it introduces the measurement techniques and setups used to characterize the different aspects of BAL performance.

A literature review is provided in chapter 3, starting with an overview of state-of-the-art BAL performance using the best results from notable 9xx nm realizations in recent publications. This is followed by brief descriptions of the important thermal and non-thermal performance-limiting mechanisms that have been identified over many years, highlighting the specific performance aspects each mechanism is associated with limiting or degrading. The chapter concludes with a review of notable lateral structuring techniques that have been developed and implemented in previous studies to confine the flow of current and charge carriers under the central BAL stripe, explaining the working principle of each technique and highlighting its benefits to BAL performance as well as its limitations and drawbacks.

Chapter 4 contains a comprehensive study (involving multiple simulations and experimental realizations) of a novel technique for current and carrier confinement based on integrating structured current-blocking layers outside the stripe. It is found that this technique successfully demonstrates simultaneously high η_{E}, B_{lat} and DoP up to high P_{opt} levels, as well as high process quality and repeatability despite relatively high complexity. The chapter begins with a detailed design study using modeling and simulation tools, starting with selecting a well-suited epitaxial structure, then optimizing the blocking layer parameters and vertical position in two design variants, and finally estimating performance benefits relative to standard gain-guided

BALs. This is followed by presenting the first successful realizations of both variants using modified wafer processes that involve two-step epitaxial growth and additional processing steps, and the results of various quality control tests carried out to verify their correct implementation. In the following step, a large number of BALs (with and without blocking layers) are mounted and characterized under continuous-wave operation. These measurement results are presented and analyzed, comparing the experimentally demonstrated performance benefits to simulation estimates, followed by benchmarking exemplary results against state-of-the-art performance. The chapter concludes with a brief summary, providing an outlook for the novel design and proposing related topics for future studies.

Chapter 5 presents a simulation-based design study of a novel lateral structuring technique which follows a different approach, namely the central confinement of heat flow (rather than current), with the aim of reducing the curvature of the lateral temperature profile around the active zone and the associated BPP_{lat} degradation. This is realized by laterally structuring certain epitaxial layers and replacing them outside the stripe with materials with low thermal conductivity, thereby engineering a chip-internal thermal path. The chapter starts with a brief review of approaches implemented in previous studies to flatten the temperature profile, presenting their benefits as well as their limitations which motivate the proposed design. This is followed by presenting a detailed two-dimensional BAL model that is used in finite-element thermal simulations, calibrated against thermal camera images, to calculate heat distribution within a mounted BAL chip under given operating conditions. Using this model, the lateral temperature profiles in multiple design variants are compared to a reference BAL (with no heat blocking), demonstrating the expected curvature reduction. This novel design has not been practically realized within the scope of this work, but the promising simulation results make it an attractive approach for future realizations of high-brightness BALs.

2

Research Methods and Techniques

This chapter is dedicated to providing an overview of the research methodology used to study the semiconductor devices that are the subject of this work, namely high-power edge-emitting broad-area diode lasers (BALs) based on GaAs. It starts with section 2.1, which introduces the software used in BAL modeling and performance simulation, followed by section 2.2, which describes the fabrication steps used to realize them and the underlying technological aspects. Finally, section 2.3 presents the measurement setups and techniques used to characterize the different performance aspects of the realized BALs.

2.1 Device modeling and simulation tools

This section provides a brief introduction to the software used in this work to model high-power BALs and simulate their different performance aspects. These simulation tools are used for design development and optimization, and for estimating the impact of novel design approaches prior to realization. Detailed descriptions of the full capabilities and the underlying mathematical framework of each tool are not provided here, instead focusing on their application within the context of this work.

The first simulation tool is a waveguide equation solver called "QIP2", that was developed at the FBH [27]. Based on the refractive index profile of a given epitaxial (vertical) layer structure, QIP2 uses the effective refractive index (n_{eff}) method, as described in [27,28], to solve the waveguide equation for the guided vertical modes and simulate their optical intensity profiles (e.g. Fig. 4.1), thereby enabling the calculation of various key parameters for each mode, including the QW optical confinement factor (Γ), internal optical loss (α_{i}), near-field width and far-field angle. Γ is defined as the fraction of the total mode intensity that overlaps with the QW, i.e.

$$\Gamma = \left[\int_{-d_{\mathrm{AZ}}/2}^{d_{\mathrm{AZ}}/2} \mathcal{I}_y(y)\, dy \right] \Big/ \left[\int_{-\infty}^{\infty} \mathcal{I}_y(y)\, dy \right], \tag{2.1}$$

where $\mathcal{I}_y(y)$ is the vertical mode intensity profile (with $y = 0$ at the QW center) and d_{AZ} is the active zone thickness [2,5,29]. Although multiple loss mechanisms contribute to α_{i}, free carrier absorption can generally be assumed to be the dominant factor [8,30,31], and can be

calculated as

$$\alpha_{\mathrm{i}}^{(\mathrm{FCA})} = \int \mathcal{I}_y(y) \frac{n(y)}{n_{\mathrm{eff}}} \left(\sigma_{\mathrm{n}} N_{\mathrm{n}}(y) + \sigma_{\mathrm{p}} N_{\mathrm{p}}(y)\right) dy, \tag{2.2}$$

with $n(y)$ as the refractive index profile, $N_{\mathrm{n}}(y)$ and $N_{\mathrm{p}}(y)$ as the electron and hole density profiles, respectively, and σ_{n} and σ_{p} as the corresponding free carrier absorption cross sections. In this simulation, α_{i} is therefore approximated as $\alpha_{\mathrm{i}} \approx \alpha_{\mathrm{i,QW}}^{(\mathrm{FCA})} + \alpha_{\mathrm{i,WG}}^{(\mathrm{FCA})}$, with the two terms corresponding to free carrier absorption in the QW and in its surrounding layers that form the optical waveguide, respectively. The first term is separately calculated by reducing equation 2.2 (assuming quasi-neutrality) to $\alpha_{\mathrm{i,QW}}^{(\mathrm{FCA})} = \Gamma N_{\mathrm{th}} (\sigma_{\mathrm{n}} + \sigma_{\mathrm{p}})$, where N_{th} is the threshold carrier density in the QW, estimated based on calculations of material gain spectra using another FBH internal software called "kp8" [29,32]. Following equation 2.2, $\alpha_{\mathrm{i,WG}}^{(\mathrm{FCA})}$ is calculated by QIP2 as the sum of contributions of all the other layers, with the loss contribution of each layer estimated by calculating its modal confinement factor (analog to equation 2.1) and replacing N_{n} and N_{p} with the corresponding doping concentration (i.e. ignoring minority carriers). For both the QW and waveguide calculations, σ_{n} and σ_{p} are given as 3.7×10^{-18} and $11 \times 10^{-18}\,\mathrm{cm}^2$, respectively, as empirically estimated in [8,33], i.e. three times higher free carrier absorption for holes (on the p-side) than for electrons (on the n-side). In addition, QIP2 also calculates the total sheet resistance of the layer structure, based on the thickness and resistivity of each layer [8,27]. Moreover, this simulation can be extended to two regions with similar but non-identical layer structures, representing the central and outer regions in a laterally-structured BAL. This enables, for example, the estimation of the lateral effective refractive index step (Δn_{eff}) and thus the expected lateral waveguiding in such devices (e.g. Figs. 4.4 and 4.9).

Another simulation tool is "WIAS-TeSCA", which was developed at the Weierstrass Institute for Applied Analysis and Stochastics (WIAS) [34,35]. For a given device cross section, it numerically solves the system of equations corresponding to the drift-diffusion model for two-dimensional charge carrier transport, as well as the Helmholtz waveguide equation for the guided vertical modes. Assuming spatial homogeneity along the longitudinal axis, the optical power ($P_{\mathrm{opt},j}$) of a vertical mode j can be calculated self-consistently by solving the rate equation

$$\frac{d}{dt} P_{\mathrm{opt},j} = v_{\mathrm{g},j} (G_j - \alpha_{\mathrm{s},j} - \gamma_j) P_{\mathrm{opt},j} + \dot{P}_{\mathrm{opt},j}^{\mathrm{spont}}, \tag{2.3}$$

where $v_{\mathrm{g},j}$ is the group velocity, G_j is the net gain (i.e. absorption losses subtracted), $\alpha_{\mathrm{s},j}$ corresponds to additional losses (mainly due to scattering), and γ_j corresponds to outcoupling mirror losses, while $\dot{P}_{\mathrm{opt},j}^{\mathrm{spont}}$ is the rate of spontaneous emission into the mode [35]. For a BAL at a given bias voltage (U), TeSCA is used in this work to calculate the corresponding current (I) and total optical power (P_{opt}), as well as the energy band diagrams and two-dimensional current and carrier density profiles along the lateral and vertical axes (e.g. Figs. 4.11 and 4.6). A simpler version of this simulation, based on using the drift-diffusion model to simulate one-dimensional carrier transport, is used to calculate the I-U characteristics of a given vertical structure, which is required in this work to enable the comparison of different current-blocking configurations (e.g. Figs. 4.2 and 4.5(a)).

The "Ansys Mechanical" finite element analysis (FEA) software is also used in this work to simulate heat distribution within BAL chips [36,37]. Following [38,39], a detailed